JOURNAL OF AIRCRAFT
Vol. 40, No. 5, September–October 2003

Prediction of Tiltrotor Height–Velocity Diagrams Using Optimal Control Theory

Eric B. Carlson*
Bell Helicopter Textron, Inc., Fort Worth, Texas 76101
and
Yiyuan J. Zhao†
University of Minnesota, Minneapolis, Minnesota 55455

Height–velocity (H–V) diagrams represent combinations of rotorcraft heights and speeds from which safe landings cannot be made in case of an engine failure. Boundary points of H–V diagrams for a tiltrotor aircraft are determined systematically using optimal control theories. A two-dimensional rigid-body model representative of the XV-15 tiltrotor aircraft is developed. The tabular aerodynamic data are interpolated with smooth functions to facilitate use in numerical optimizations. An optimal control problem is formulated that minimizes a linear combination of the height and speed at an engine failure, such that subsequent control actions can still land the tiltrotor aircraft with acceptable touchdown speeds and pitch attitudes. Path constraints are imposed on the control variables, their rates, and on state variables to reflect realistic flight limitations. This optimal control problem is converted into a parameter optimization via a collocation approach, and is numerically solved with the software NPSOL. Height–velocity diagrams are calculated by solving this optimal control problem repeatedly. The cases one-engine inoperative and all-engines failed are both considered. Effects of the gross weight variations on H–V diagrams are studied. Optimal landing flights for engine failures occurring on the boundaries of H–V diagrams are discussed. Sensitivity analyses are conducted to examine effects of various modeling errors on optimization results.

Nomenclature

A_x = x component of aerodynamic force in body reference frame
A_z = z component of aerodynamic force in body reference frame
C_P = required power coefficient
C_T = single rotor thrust coefficient
c_d = average rotor blade drag coefficient
c_w = mean wing chord, ft
D = drag, lb
d = distance between nacelle rotation point and hub center
f_G = ground effect factor
g = acceleration due to gravity, ft/s^2
h = tiltrotor altitude, ft
h_R = above c.g. location of nacelle rotation point
$h_{()}$ = above c.g. location of a specific aerodynamic center
I = performance index of optimal control problem
I_R = rotor polar moment of inertia, slug · ft^2
I_y = pitch moment of inertia, slug · ft^2
i_n = nacelle angle
K_{ind} = induced power factor, >1
L = lift, lb
l_R = behind c.g. location of nacelle rotation point
$l_{()}$ = behind c.g. location of a specific aerodynamic center
M = aerodynamic pitching moment, lb · ft
m = tiltrotor mass
P_{AEO} = all-engines operating power rating
P_a = power available, lb · ft/s
P_{OEI} = one-engine power rating when the other engine is inoperative
P_r = power required, lb · ft/s
q = pitch rate, rad/s; with subscript, dynamic pressure
R = rotor radius, ft
S = generic reference area, ft^2
s = longitudinal stick displacement, in.
T = thrust from one rotor, lb
t_f = final time of the optimization problem, s
t_p = power available time constant, s
U_c = flow perpendicular to rotor plane, ft/s
U_t = flow parallel to rotor plane, ft/s
u = horizontal velocity component in body axes, ft/s
V = airspeed
v_i = induced velocity, ft/s
W = gross weight, lb
w = vertical velocity component in body reference frame, positive down, ft/s
x = horizontal location of aircraft
α = angle of attack, rad
β = cyclic angle, rad
γ = flight-path angle
δ_e = elevator deflection, rad
δ_{fl} = flap angle
η_h = horizontal stabilizer flow reduction factor
η_i = rotor-induced velocity development factor
η_p = power consumption correction factor
θ = pitch angle, rad
μ = advance ratio
ρ = air density, slug/ft^3
σ = rotor solidity ratio
Ω = rotor speed, rad/s
Ω_0 = nominal rotor speed

Subscripts

f = relating to fuselage
fs = in free stream

Received 20 January 2003; revision received 9 June 2003; accepted for publication 9 June 2003.

*Engineering Specialist, Aerodynamics, P.O. Box 482; ecarlson@bellhelicopter.textron.com.
†Associate Professor, Aerospace Engineering and Mechanics; gyyz@aem.umn.edu. Senior Member AIAA.

hs = relating to horizontal stabilizer
ss = in rotor slip stream
w = relating to wing

Superscripts

$\cdot$ = time derivative
$'$ = derivative with respect to normalized time
$-$ = normalized variable

I. Introduction

TILTROTOR aircraft are designed to combine the advantages of both helicopter and turbo-prop airplanes. They can take off and land like helicopters, requiring short runways. Once airborne, they can tilt their rotors forward to fly like turboprop airplanes. Several versions of tiltrotor aircraft have been designed and flown[1–8] including the Bell XV-3 convertiplane, the Bell XV-15 tiltrotor research aircraft, and the Bell/Boeing V-22 Osprey. The Bell/Agusta Aerospace Company has started to build the commercial tiltrotor aircraft B609, which is a six to nine passenger tiltrotor similar in size and design to the XV-15.

Civil tiltrotor aircraft must demonstrate satisfactory flight characteristics in the event of engine failure, to be certified by the Federal Aviation Administration (FAA). There are two possible engine failure situations; one-engine inoperative (OEI) and all-engines inoperative (AEI). In the event of an OEI, a tiltrotor aircraft may either continue flight or land safely, depending on the weight, power available, and vehicle states at engine failure. In the event of an AEI, on the other hand, landing is inevitable. In both cases, rotorcraft pilots can make safe landings if vehicle states and ambient conditions are favorable.

On the other hand, there is a region of unsafe flight states and ambient conditions from which even skilled pilots may not be able to land a rotorcraft safely in the event of engine failure. For a given weight and ambient conditions, this unsafe region is often described by a combination of rotorcraft height and speed at the point of engine failure and is called a height–velocity (H–V) diagram, or a deadman's curve. The determination of H–V diagrams at various gross weights and ambient conditions are very important to safe rotorcraft operations. The H–V diagrams show pilots which conditions to stay away from during normal operations, so that the rotorcraft can survive an unexpected engine failure. They are also used to define nominal takeoff and landing operation procedures.

In the past, these curves have been determined with dangerous, time consuming, and expensive flight tests. Pilots have in fact lost their live determining these curves. In these flight tests, pilots simulate an engine failure at certain initial altitude and speed and try to make a safe landing. These initial conditions are varied systematically until pilots no longer feel able to make a safe landing. In Ref. 9, Okuno et al. showed how optimal control theory can be used to determine three key points on the low-speed H–V diagram of a helicopter. Other research efforts on optimal rotorcraft flight trajectories in engine failure can be found in Refs. 10–21.

In this paper, optimal control theory is used to determine the low-speed H–V diagrams for a tiltrotor aircraft based on the XV-15 model. In addition, a modified performance index is used for the optimal control formulation so that all points on the low speed H–V diagram can be determined. Results of this paper can be used as references for flight tests to improve safety and reduce time and cost.

Specifically, a two-dimensional rigid-body model of a tiltrotor aircraft is developed, which employs a full range of aerodynamic data for the XV-15 interpolated with smooth functions. Download on the wing is modeled by considering the parts of the wing in the freestream and in slip stream separately. An optimal control problem is formulated to determine a combination of height and velocity on the boundary of an H–V diagram. This optimal control problem is converted into parameter optimization for numerical solutions. Then, boundary points on H–V diagrams are systematically calculated for various gross weights and different engine failure conditions. Optimal landing flights in engine failures occurring on H–V diagram boundaries are discussed. Finally, sensitivity analyses are conducted to examine effects of model parameter variations on optimal solutions.

II. Tiltrotor Aircraft Modeling

To determine H–V diagrams for a tiltrotor aircraft using optimal control theory, a mathematical model of the tiltrotor must first be established. Results of this paper are based on the configuration and parameters of the XV-15 tiltrotor aircraft because it has been well researched. The XV-15 was a joint U.S. Army/NASA/U.S. Navy proof-of-concept project begun in the 1970s.[2–4] It has a design gross weight of 13,000 lb and a maximum gross weight of 15,000 lb. Its two three-bladed, 25-ft-diam rotors have highly twisted blades which twist 45 deg root to tip. The nacelles can tilt from 0 to 95 deg; with 0 being the airplane mode and 90 deg being the helicopter mode. References 2–6 contain dimensions of the XV-15 aircraft. The control system consists of four separate subsystems[7]: primary flight controls, secondary flight controls, automatic flight controls, and the thrust/power management system.

The tiltrotor is a symmetric vehicle, and main motions of optimal landing flights in the event of engine failure are in the vertical plane. Therefore, only longitudinal dynamics need to be considered. An appropriate two-dimensional longitudinal tiltrotor model must account for forces and moments produced by the rotors, the wing, the fuselage, and the horizontal stabilizer. This is important because the pilot stick control affects both the rotor thrust inclination and the elevator deflection. Also, because a tiltrotor can fly like a helicopter, forces and moments for all aerodynamic surfaces and the fuselage must be modeled for the full range of angle of attack, between -180 and 180 deg.

Figure 1 shows a free-body diagram for the two-dimensional rigid-body tiltrotor model. The corresponding equations of motion are developed in Ref. 21 and are summarized as follows:

$$\dot{w} = 1/m[A_z - 2T\sin(i_n - \beta)] + g\cos\theta + qu \tag{1}$$

$$\dot{u} = 1/m[A_x + 2T\cos(i_n - \beta)] - g\sin\theta - qw \tag{2}$$

$$\dot{\theta} = q \tag{3}$$

$$\dot{q} = 1/I_y\{M - 2T[l_R\sin(i_n - \beta) + h_R\cos(i_n - \beta) + d\sin\beta]\} \tag{4}$$

$$\dot{\Omega} = 1/I_R[(P_a - P_r)/\Omega] \tag{5}$$

$$\dot{h} = u\sin\theta - w\cos\theta \tag{6}$$

$$\dot{x} = u\cos\theta + w\sin\theta \tag{7}$$

where in-plane components of the rotor forces are neglected. Model parameters used in the optimization studies are summarized in the

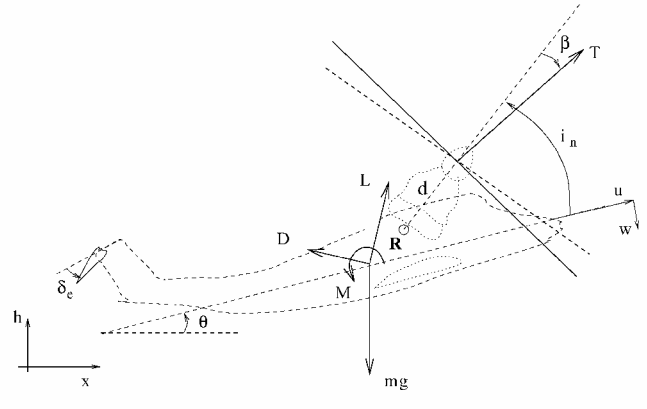

Fig. 1 Two-dimensional tiltrotor aircraft free-body diagram.

Appendix. The total forces and moment are obtained by summing up forces and moments from the rotors, the wing, the fuselage, and the horizontal stabilizer,

$$\begin{aligned} A_z &= A_{f_z} + A_{w_{\mathrm{fs}_z}} + A_{w_{\mathrm{ss}_z}} + A_{\mathrm{hs}_z} \\ &= -L_f \cos\alpha_f - D_f \sin\alpha_f - L_{w_{\mathrm{fs}}} \cos\alpha_{w_{\mathrm{fs}}} - D_{w_{\mathrm{fs}}} \sin\alpha_{w_{\mathrm{fs}}} \\ &\quad - L_{w_{\mathrm{ss}}} \cos\alpha_{w_{\mathrm{ss}}} - D_{w_{\mathrm{ss}}} \sin\alpha_{w_{\mathrm{ss}}} - L_{\mathrm{hs}} \cos\alpha_{\mathrm{hs}} \end{aligned} \tag{8}$$

$$\begin{aligned} A_x &= A_{f_x} + A_{w_{\mathrm{fs}_x}} + A_{w_{\mathrm{ss}_x}} + A_{\mathrm{hs}_x} \\ &= L_f \sin\alpha_f - D_f \cos\alpha_f + L_{w_{\mathrm{fs}}} \sin\alpha_{w_{\mathrm{fs}}} - D_{w_{\mathrm{fs}}} \cos\alpha_{w_{\mathrm{fs}}} \\ &\quad + L_{w_{\mathrm{ss}}} \sin\alpha_{w_{\mathrm{ss}}} - D_{w_{\mathrm{ss}}} \cos\alpha_{w_{\mathrm{ss}}} + L_{\mathrm{hs}} \sin\alpha_{\mathrm{hs}} \end{aligned} \tag{9}$$

$$\begin{aligned} M &= M_f + l_f A_{f_z} - h_f A_{f_x} + M_w + l_w \left(A_{w_{\mathrm{fs}_z}} + A_{w_{\mathrm{ss}_z}}\right) \\ &\quad - h_w \left(A_{w_{\mathrm{fs}_x}} + A_{w_{\mathrm{ss}_x}}\right) + l_{\mathrm{hs}} A_{\mathrm{hs}_z} - h_{\mathrm{hs}} A_{\mathrm{hs}_x} \end{aligned} \tag{10}$$

In the preceding equations,

$$L_{w_{()}} = q_{w_{()}} S_{w_{()}} C_{L_w}\left(\alpha_{w_{()}}, \delta_{\mathrm{fl}}\right) \tag{11}$$

$$D_{w_{()}} = q_{w_{()}} S_{w_{()}} C_{D_w}\left(\alpha_{w_{()}}, \delta_{\mathrm{fl}}\right) \tag{12}$$

$$M_w = \left(q_{w_{\mathrm{fs}}} S_{w_{\mathrm{fs}}} + q_{w_{\mathrm{ss}}} S_{w_{\mathrm{ss}}}\right) c_w C_{M_w}(i_n, \delta_{\mathrm{fl}}) \tag{13}$$

$$L_{\mathrm{hs}} = q_{\mathrm{hs}} S_{\mathrm{hs}} C_{L_{\mathrm{hs}}}(\alpha_{\mathrm{hs}}, \delta_e) \tag{14}$$

where ( ) = fs or ss representing freestream or slipstream, and

$$q_f = \tfrac{1}{2}\rho\left[(u - qh_f)^2 + (w + ql_f)^2\right]$$

$$\alpha_f = \sin^{-1}\left(\frac{w + ql_f}{\sqrt{(u - qh_f)^2 + (w + ql_f)^2}}\right)$$

$$q_{w_{\mathrm{fs}}} = \tfrac{1}{2}\rho\left[(u - qh_w)^2 + (w + ql_w)^2\right]$$

$$\alpha_{w_{\mathrm{fs}}} = \tan^{-1}\left(\frac{w + ql_w}{u - qh_w}\right)$$

$$\begin{aligned} q_{w_{\mathrm{ss}}} &= \tfrac{1}{2}\rho\left[(u - qh_w + \eta_i v_i \cos(i_n - \beta))^2\right. \\ &\quad \left. + (w + ql_w - \eta_i v_i \sin(i_n - \beta))^2\right] \end{aligned}$$

$$\alpha_{w_{\mathrm{ss}}} = \tan^{-1}\left[\frac{w + ql_w - \eta_i v_i \sin(i_n - \beta)}{u - qh_w + \eta_i v_i \cos(i_n - \beta)}\right]$$

$$q_{\mathrm{hs}} = \tfrac{1}{2}\eta_h \rho\left[(u - qh_{\mathrm{hs}})^2 + (w + ql_{\mathrm{hs}})^2\right]$$

$$\alpha_{\mathrm{hs}} = \tan^{-1}\left(\frac{w + ql_{\mathrm{hs}}}{u - qh_{\mathrm{hs}}}\right)$$

Because part of the wing is in the rotor slipstream and part is in the freestream, it experiences different flow velocities at its two different parts. As an approximation, the wing's contribution to the force and pitching moment is developed in two separate parts, one for the portion of the wing in the slipstream and one for the portion in the freestream. In this paper, a simplified equation dependent on nacelle angle and forward speed is employed to calculate areas of the wing under the slipstream influence,[21]

$$S_{w_{\mathrm{ss}}} = \begin{cases} 0 & i_n < 60 \text{ deg or } u \geq u_{\mathrm{cr}} \\ S_{\mathrm{ss}_{\max}}[\sin(ai_n) + \cos(bi_n)]\dfrac{(u_{\mathrm{cr}} - u)}{u_{\mathrm{cr}}} & \text{else} \end{cases} \tag{15}$$

where $S_{\mathrm{ss}_{\max}} = 2\eta_{\mathrm{ss}} R c_w$, $\eta_{\mathrm{ss}} < 1$, and u_{cr}, a, and b are selected to match experimental data. In this paper, $u_{\mathrm{cr}} = 40$ ft/s, $a = 1.386$, and $b = 3.114$. Once the area of the wing under the slipstream influence is determined,

$$S_{w_{\mathrm{fs}}} = S_w - S_{w_{\mathrm{ss}}} \tag{16}$$

The tiltrotor wake impingement on the wing (download) and, accordingly, aerodynamic forces of the wing mainly depend on the angle of attack. During an OEI flight maneuver, the tiltrotor wing may go in and out of stall. The aerodynamic data used in this paper account for this phenomenon.

When engine failure occurs, the power available changes from the normal all-engine operating rating to $P_{\mathrm{AEI}} = 0$ in a total power failure, or to a single-engine contingency rating P_{OEI} in one engine inoperation,

$$P_a = (P_{\mathrm{AEO}} - P_{\mathrm{OEI,AEI}}) \exp(-t/t_p) + P_{\mathrm{OEI,AEI}} \tag{17}$$

The power required P_r and the single rotor thrust can be expressed as[22–24]

$$P_r = (2/\eta_p)\rho(\pi R^2)(\Omega R)^3 C_P = (2/\eta_p)\rho\pi R^5 \Omega^3 C_P \tag{18}$$

$$T = \rho(\pi R^2)(\Omega R)^2 C_T = \rho\pi R^4 \Omega^2 C_T \tag{19}$$

where a power factor $\eta_p < 1$ is used to account for power losses in the transmission.[23] The required power coefficient for a single rotor is computed from

$$C_P = C_T\sqrt{C_T/2}(K_{\mathrm{ind}} f_G \bar{v}_i + \bar{U}_c) + \tfrac{1}{8}\sigma c_d(1 + 4.7\mu^2) \tag{20}$$

where

$$v_h = \sqrt{T/2\rho\pi R^2} = \Omega R\sqrt{C_T/2}$$

$$\begin{aligned} \bar{U}_c &= [(u - qh_R)\cos(i_n - \beta) \\ &\quad - (w + ql_R)\sin(i_n - \beta) - qd\sin\beta]/v_h \end{aligned}$$

$$\begin{aligned} \bar{U}_t &= [(u - qh_R)\sin(i_n - \beta) \\ &\quad + (w + ql_R)\cos(i_n - \beta) - qd\cos\beta]/v_h \end{aligned}$$

$$\mu = v_h \bar{U}_t/\Omega R = \bar{U}_t\sqrt{C_T/2}$$

The normalized rotor induced velocity $\bar{v}_i = v_i/v_h$ is determined as follows. When rotor flows are outside of the vortex-ring state, $(2\bar{U}_c + 3)^2 + \bar{U}_t^2 > 1$, it is given by the momentum theory,[22–24]

$$\bar{v}_i^4 + 2\bar{U}_c^2 \bar{v}_i^3 + \left(\bar{U}_c^2 + \bar{U}_t^2\right)\bar{v}_i^2 = 1 \tag{21}$$

This equation is solved with a modified Newton–Raphson scheme with a stepsize of 0.75 and the initial guess of $\bar{v}_i = 1$. For rotor flows inside the vortex-ring state, $(2\bar{U}_c + 3)^2 + \bar{U}_t^2 \leq 1$, the normalized induced velocity is given by an empirical approximation by Johnson,[11]

$$\bar{v}_i = \bar{U}_c\left(0.373\bar{U}_c^2 + 0.598\bar{U}_t^2 - 1.991\right) \tag{22}$$

This equation is included here for completeness, but in practice, the vortex-ring state should be avoided by tiltrotor configurations. In the current study, the ground effect is neglected: $f_G = 1$.

For the XV-15 aircraft, the rotor cyclic angle and elevator deflection can be related to the longitudinal stick displacement through

$$\beta = (s/s_{\max})\beta_{\max}\sin(i_n) \tag{23}$$

$$\delta_e = (s/s_{\max})\delta_{e_{\max}} \tag{24}$$

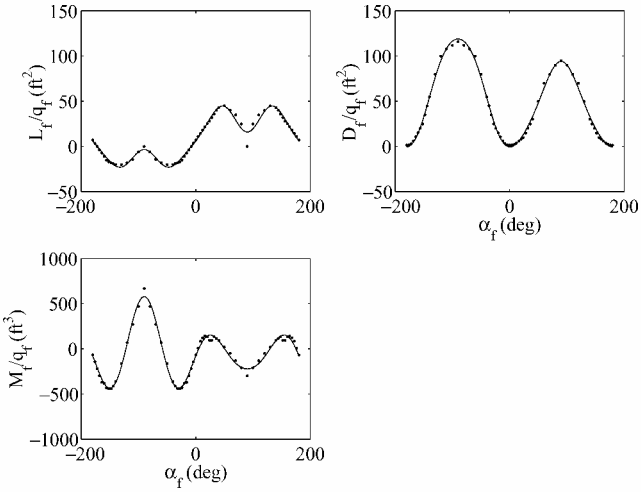

Fig. 2 Fitting of fuselage aerodynamic coefficients.

Equation (23) reflects the control phasing out as the nacelle angle changes and represents an approximation to Fig. 13 in Ref. 7 (p. 1042-9). It shows that the rotor cyclic β is in full effect in the helicopter mode, $i_n = 90$ deg, and is always zero in the airplane mode, $i_n = 0$ deg.

The following aerodynamic coefficients are needed to determine the aerodynamic forces and moments:

$$\bar{L}_f(\alpha_f) \triangleq L_f/q_f, \qquad \bar{D}_f(\alpha_f) \triangleq D_f/q_f, \qquad \bar{M}_f(\alpha_f) \triangleq M_f/q_f \tag{25}$$

$$C_{L_w}(\alpha_w, \delta_{\mathrm{fl}}), \qquad C_{D_w}(\alpha_w, \delta_{\mathrm{fl}}), \qquad C_{M_w}(i_n, \delta_{\mathrm{fl}}), \qquad C_{L_{\mathrm{hs}}}(\alpha_{\mathrm{hs}}, \delta_e) \tag{26}$$

The available aerodynamic data for the XV-15 are given in tabular forms in Ref. 6 for the full angle-of-attack range (from -180 to 180 deg), different nacelle angles (from 0 to 95 deg), and different flap angles (0, 20, 40, and 75 deg). Because efficient optimization algorithms prefer sufficiently differentiable functions, the complicated tabular data are fit nicely with cubic splines, and in some cases with least-squares fits to power and sinusoidal terms in this paper. For example, fuselage aerodynamic coefficients are fit to sinusoidal functions plus a constant term. The lift coefficient of the fuselage required five sinusoidal terms. The fuselage drag coefficient required six terms, and the fuselage moment coefficient used seven terms. Figure 2 shows the results of these fittings. Other aerodynamic coefficients are functions of two variables. Interpolations of these aerodynamic coefficients are presented by Carlson.[21]

The validity of the preceding two-dimensional rigid-body model may be examined by studying steady-state flight conditions. During a steady-state horizontal forward flight, $\dot{w} = \dot{u} = \dot{q} = \dot{h} = \dot{\Omega} = 0$. Eqs. (1–7) result in

$$0 = A_z - 2T\sin(i_n - \beta) + mg\cos\theta \tag{27}$$

$$0 = A_x + 2T\cos(i_n - \beta) - mg\sin\theta \tag{28}$$

$$0 = M - 2T[l_R\sin(i_n - \beta) + h_R\cos(i_n - \beta) + d\sin\beta] \tag{29}$$

$$0 = u\sin\theta - w\cos\theta \tag{30}$$

$$P_r \le P_{a,\max} \tag{31}$$

where Eq. (31) actually is not needed because, in a nominal operation, the engine provides just as much power as is required, that is, $P_a = P_r$ and $\bar{\Omega} = 1.0$. For specified values of u, i_n, and δ_{fl}, together with $q = 0$ and $\bar{\Omega} = 1$, these equations are solved to obtain values of w, θ, C_T, and s. Table 1 shows examples of steady-state flight conditions determined from preceding equations. Values of these conditions are reasonable for the tiltrotor. These steady-state values

Table 1 Steady-state horizontal flight conditions

w, kn	u, kn	θ, deg	$2T$, lb	$\bar{s}$
0.00	0.00	−3.44	13,870	−0.26
−0.51	10.00	−2.94	13,470	−0.25
−1.00	20.00	−2.87	13,010	−0.22
−2.22	40.00	−3.18	12,510	−0.16

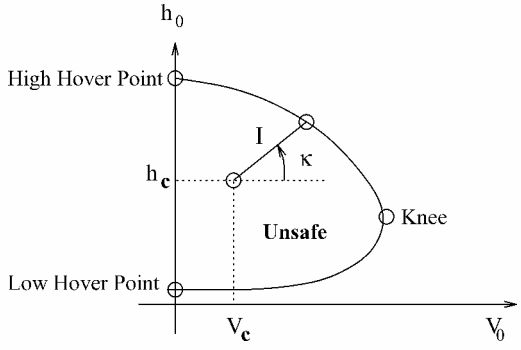

Fig. 3 Typical low-speed helicopter H–V diagram.

can be used to calculate the power required in Eq. (18). Calculated powers agree well with flight-test powers over low-speed regimes in the helicopter mode and medium speeds with fairly large nacelle angles (usually $60 \le i_n \le 95$ deg) in the conversion mode. In other words, the model developed predicts correct trends of the power required as functions of airspeed and nacelle angles. Details are omitted and can be found in Ref. 21.

The following normalization and scaling are used in all numerical computations in this paper:

$$\bar{w} = 100w/\Omega_o R, \qquad \bar{u} = 100u/\Omega_o R, \qquad \bar{h} = h/R$$

$$\bar{x} = x/R, \qquad \bar{q} = 100q/\Omega_o, \qquad \bar{\Omega} = \Omega/\Omega_o \tag{32}$$

The scaled and normalized control variables are

$$\bar{C}_T \triangleq 10^4(2\rho\pi R^3/m)C_T, \qquad \bar{s} \triangleq s/s_{\max} \tag{33}$$

Finally, the normalized time and the derivative with respect to it are defined as

$$\tau = \frac{0.01}{1/\Omega_o}t = 0.01\Omega_o t, \qquad ()' = \frac{\mathrm{d}()}{\mathrm{d}\tau} \tag{34}$$

In the preceding equation, the factor of 100 is selected to bring normalized variables close to one for good numerical efficiency in the optimization studies.

III. Problem Formulations

Procedures for safely landing a helicopter in case of an engine failure have been well established over the years.[25] With right combinations of the helicopter height and speed at an engine failure, the pilot can cleverly manage the helicopter energy to bring it down safely without damaging people or the machine. However, there exist some helicopter flight conditions from which safe landings simply cannot be made in engine failure, even by highly skilled pilots. The H–V diagram (or deadman's curve) represents combinations of such heights and speeds. Figure 3 shows the low-speed region of a typical helicopter H–V diagram in the event of a total engine failure.[25]

There are three definite points in a H–V diagram: the low-hover point, the high-hover point, and the knee. For engine failures up to the low-hover point, the pilot can come straight down and use collective pitch to cushion the landing as the rotor slows down. For engine failures above the low-hover point, the rotor will either slow down and stall if the pilot does not reduce the collective pitch, or the helicopter will hit too hard if the pilot does. For engine failures above the high-hover point, there is a sufficient altitude to make a diving transition into a forward flight autorotation and execute a power-off flare. If the speed at an engine failure exceeds the knee

of the curve, an engine failure is survivable because of the adequate initial kinetic energy.

Before efforts are made to determine H–V diagrams for a tiltrotor aircraft, an exploratory optimization problem is first solved to test whether a H–V diagram exists for a tiltrotor aircraft. Consider the following problem in the event of an engine failure,

$$\min I = K\bar{w}^2(t_f) + \bar{u}^2(t_f) \tag{35}$$

subject to normalized versions of Eqs. (1–7), the following path constraints

$$\theta_{\min} \le \theta \le \theta_{\max}, \qquad \bar{\Omega}_{\min} \le \bar{\Omega} \le \bar{\Omega}_{\max}, \qquad \bar{h} \ge 0 \tag{36}$$

$$\bar{C}_{T_{\min}} \le \bar{C}_T \le \bar{C}_{T_{\max}}, \qquad |\bar{s}| \le 1, \qquad 0 \le i_n \le 95 \text{ deg} \tag{37}$$

$$|\bar{C}_T|' \le \bar{C}'_{T_{\max}}, \qquad |\bar{s}|' \le \bar{s}'_{\max}, \qquad |i|'_n \le i'_{n_{\max}} \tag{38}$$

and the following terminal constraints,

$$\bar{h}(t_f) = 0 \tag{39}$$

$$\theta_{f,\min} \le \theta(t_f) \le \theta_{f,\max} \tag{40}$$

where $K > 0$ is a weighting factor. This problem essentially determines the smallest possible touchdown speeds in an engine failure. Systematic variations are made in h_0 and V_0 at the engine failure, as well as in the gross weight W. These studies indicate that the touchdown speeds become excessive for certain combinations of initial heights and speeds. In other words, a H–V region like that of a helicopter exists for the XV-15 tiltrotor. Details are omitted.

We now apply optimal control theories to determine H–V diagrams for the XV-15 tiltrotor aircraft. Normally, H–V diagrams are determined as functions of the gross weight and ambient conditions, with the assumptions of average piloting skills and steady-state conditions at engine failure. Essentially, boundary points of H–V diagrams represent conditions from which a safe landing can barely be made in case of an engine failure. In a landing flight after an engine failure, structural damages can be caused by excessive speeds at touchdown and/or out-of-range attitudes. Therefore, the following optimal control problem is formulated to determine one point on the boundary of an H–V diagram (Fig. 3):

$$\min I = (\bar{V}_0 - \bar{V}_c)\cos\kappa + (\bar{h}_0 - \bar{h}_c)\sin\kappa \tag{41}$$

subject to normalized versions of Eqs. (1–7), path constraints in Eqs. (36–38), the initial boundary condition,

$$(\bar{h}_0 - \bar{h}_c)\cos\kappa = (\bar{V}_0 - \bar{V}_c)\sin\kappa \tag{42}$$

and the following terminal constraints,

$$\bar{h}(t_f) = 0 \tag{43}$$

$$\theta_{f,\min} \le \theta(t_f) \le \theta_{f,\max} \tag{44}$$

$$\bar{u}(t_f) \le \bar{u}_{\max} \tag{45}$$

$$\bar{w}(t_f) \le \bar{w}_{\max} \tag{46}$$

$$i_n(t_f) \ge 60 \text{ deg} \tag{47}$$

This problem minimizes the distance along a straight line originating from a pre-selected reference point (V_c, h_c) inside the unsafe H–V region (Fig. 3). The condition in Eq. (42) constrains the initial height and speed to the straight line defined by the angle κ. Terminal conditions in Eqs. (43–46) specify marginally safe landings. Equation (47) limits the nacelle angle to be above 60 deg so that rotor will not strike the ground. Parameters V_c and h_c in the preceding formulations can be selected to increase the numerical accuracy in determining a boundary point on the H–V diagram, by making the line from (V_c, h_c) to a target boundary point as perpendicular as possible to the H–V diagram contour. In all results reported in this paper, the reference velocity V_c is chosen to be zero. Different reference heights h_c are chosen to be approximately in the middle of the high-hover and low-hover points.

The problem begins at the moment of engine failure, at which the aircraft is assumed to be flying in a level steady-state flight. Pilot delay is not included in the nominal results, but studied in a sensitivity analysis to follow. The pilot is assumed to have switched the rotor speed governor off at the moment of engine failure detection, so that rotor energy can be properly managed during the landing process. This formulation can be solved repeatedly for different values of the angle κ and the gross weight W to produce a contour of the H–V diagram.

IV. Numerical Solution Methods

There exist many numerical methods for solving the described problem, which may defy analytical solutions due to its complicated nature. A highly effective numerical solution approach is to convert these optimal control problems into parameter optimization problems[26–28] and then employ mature nonlinear programming codes. In particular, the collocation method converts both state and control variables into parameters and is very flexible. This method is used here, and the resulting parameter optimization problems are solved with the software package NPSOL.[29]

The conversion of an optimal control problem into a parameter optimization using a collocation approach begins with the definition of a series of nn time points within the solution time interval $[t_0, t_f]$ of an optimal control problem. Define

$$0 = \tau_1 < \tau_2 < \tau_3 < \cdots \tau_{nn-1} < \tau_{nn} = 1 \tag{48}$$

In case of equally spaced points,

$$h_k = 1/(nn-1) \tag{49}$$

and for $k = 1, 2, \ldots, nn$,

$$\tau_k = (k-1)h_k \tag{50}$$

Then

$$t_k = t_f\ \tau_k \tag{51}$$

Values of the state and control variables at each time point become solution variables. The corresponding discretized solution parameters are represented by

$$x_1^i, \ldots, x_k^i, \ldots, x_{nn}^i \tag{52}$$

$$u_1^j, \ldots, u_k^j, \ldots, u_{nn}^j \tag{53}$$

where $x_k^i = x^i(t_k)$ is the ith component of the state vector $\boldsymbol{x}$ evaluated at t_k, $u_k^j = u^j(t_k)$ is the jth component of the control vector $\boldsymbol{u}$ evaluated at t_k for $i = 1, \ldots, 7$, $j = 1, 2, 3$. Putting all of the unknown variables together and including the open final time, we have

$$\boldsymbol{X} = \left[x_1^1, \ldots, x_{nn}^1, \ldots, x_{nn}^7, u_1^1, \ldots, u_{nn}^1, \ldots, u_{nn}^3, t_f\right] \tag{54}$$

which has $N = (7+3)nn + 1$ components.

The seven differential equations in Eqs. (1–7) are converted into $7(nn-1)$ nonlinear equality constraints on these solution parameters. Specifically, these differential equations may be symbolically expressed as

$$\dot{\boldsymbol{x}} = \boldsymbol{f}(\boldsymbol{x}, \boldsymbol{u}, \boldsymbol{p}, t) \tag{55}$$

for $i = 1, 2, \ldots, 7$. For $k = 1, 2, \ldots, nn-1$ then define

$$\boldsymbol{x}_m = \tfrac{1}{2}(\boldsymbol{x}_k + \boldsymbol{x}_{k+1}) - \tfrac{1}{8}(\boldsymbol{f}_{k+1} - \boldsymbol{f}_k)(\tau_{k+1} - \tau_k)t_f \tag{56}$$

$$\boldsymbol{u}_m = \tfrac{1}{2}(\boldsymbol{u}_k + \boldsymbol{u}_{k+1}) \tag{57}$$

$$t_m = \tfrac{1}{2}(\tau_k + \tau_{k+1})t_f \tag{58}$$

Using Simpson's one-third rule, the resulting equality constraints can be expressed as

$$C_{k+(i-1)(nn-1)} = \boldsymbol{x}^i_{k+1} - \boldsymbol{x}^i_k - \tfrac{1}{6}\left(f^i_k + 4f^i_{m,k} + f^i_{k+1}\right)(t_{k+1} - t_k) \tag{59}$$

The path constraints in Eqs. (36) and (37) are enforced at the series of discrete time points as bounds on the solution parameters. To satisfy Eq. (38), a forward difference scheme is used to represent time derivatives of the control variables. Fixed initial-state conditions are enforced by equating upper and lower bounds on the corresponding variables, whereas Eq. (42) is treated as a nonlinear equality constraint. The terminal conditions in Eqs. (43–47) are met through bounds on the corresponding solution variables.

The converted parameter optimization problem may be stated in the following general form:

$$\min_{\boldsymbol{X} \in R^N} F(\boldsymbol{X}) \tag{60}$$

subject to

$$\boldsymbol{L} \le \begin{Bmatrix} \boldsymbol{X} \\ A_L \boldsymbol{X} \\ \boldsymbol{C}(\boldsymbol{X}) \end{Bmatrix} \le \boldsymbol{U} \tag{61}$$

where $\boldsymbol{X}$ is the solution parameter vector, R^N is the N-dimensional real space, $F(\boldsymbol{X})$ is a nonlinear objective function, A_L is an $m_L \times N$ constant matrix of general linear constraints, and $\boldsymbol{C}(\boldsymbol{X})$ is an m_N vector of nonlinear constraint functions. The upper and lower bounds $\boldsymbol{L}$ and $\boldsymbol{U}$ are specified for all of the solution variables and for all of the constraints. This problem can be solved efficiently using the NPSOL program.[29] In this paper, gradients for both the objective functions and the nonlinear constraints are calculated numerically. Different numbers of time interval divisions are experimented. In obtaining numerical solutions, constant initial guesses for the state and control variables are used.

V. H–V Diagrams in OEI

Figure 4 shows calculated H–V diagrams in one-engine failure at four different gross weights. Standard sea-level atmospheric conditions are assumed. Other parameters used in the optimization studies are given in the Appendix. These diagrams are similar in shapes to typical helicopter H–V diagrams obtained with flight tests.[25] As the weight decreases, the curve contracts in all directions.

Many things can be learned from Fig. 4 about feasibilities of different types of tiltrotor takeoff and landing procedures. There are basically three types of tiltrotor takeoff operations. In a vertical takeoff, a tiltrotor would climb vertically at a small speed to a certain height and then climbs out if everything is normal. In a runway takeoff, a tiltrotor would accelerate on the runway to a certain liftoff speed and then climbs out. In an oblique takeoff, the tiltrotor would lift off the ground to a few feet to hover in ground effect and then accelerates in ground effect to a certain speed and climbs out. Similar landing procedures can be defined. During normal all engine operating flights, the runway operation allows a tiltrotor to carry the largest gross weight, and the vertical operation allows a tiltrotor to carry the least gross weight. This is also true in the event of an engine failure, as indicated from Fig. 4.

In Fig. 4, the information shown suggests that, at some weight, the H–V curve consists of merely a point. This is the weight at which vertical operations are safe in the event of OEI, because, at this weight, the tiltrotor can make a safe landing in case of one-engine failure even at zero initial speed. This weight is somewhat less than 12,000 lb for the XV-15, as shown in Fig. 4. During practical vertical operations, tiltrotor aircraft usually have a certain small speed, although the velocity vector may be backward in a backup vertical takeoff procedure. If the possibility of one engine failure needs to be considered, in Fig. 4, the maximum safe gross weight suggested for the XV-15 during a vertical operation is around 12,000 lb.

The H–V diagram corresponding to $W = 15,000$ lb has a knee speed of about 26 kn. Therefore, the XV-15 should not attempt a vertical operation with this maximum gross weight because it does not have sufficient speed to make a safe landing in the event of OEI. On the other hand, the tiltrotor can use a runway takeoff operation to carry the maximum gross weight. In this case, the nominal takeoff liftoff speed and climbout path should be outside the H–V diagram. Takeoff and landing procedures for other gross weights can be similarly selected.

Note that in these discussions, adequate runway length is assumed to be available. Limitations in heliport dimensions further affect the maximum gross weight feasible for a tiltrotor operation.

VI. Characteristics of Landing Flights after OEI

Optimal landing flights in single-engine failures occurring on boundaries of the H–V diagrams are now investigated. A gross weight of 14,000 lb is used. Three representative points on the H–V diagrams are considered: the high–hover point, the knee point, and the low-hover point (Fig. 3). Figures 5 and 6 show a comparison of optimal landing flight trajectories in OEI corresponding to single-engine failures occurring at the high-hover point, the knee point, and the low-hover point.

At the high-hover point, the initial speed is small or zero, but the height provides sufficient potential energy for a safe landing. In achieving a safe landing, the tiltrotor aircraft initially tries to build up a sufficient speed to reduce the power consumption and then uses available energy sources to perform a soft landing toward the end. When the engine failure occurs, the nacelle angle decreases initially to increase the forward speed. The vertical speed increases somewhat initially, as the aircraft enters into a diving motion. The

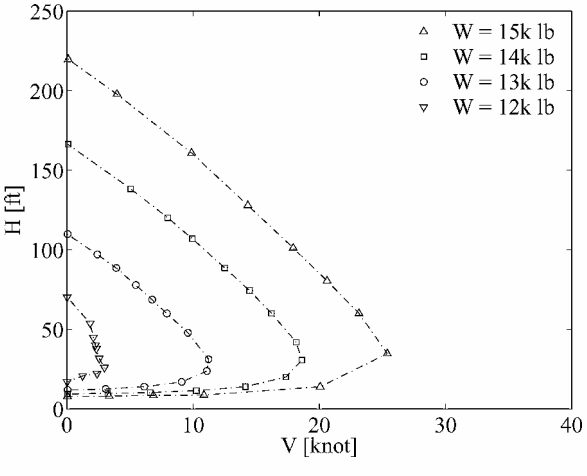

Fig. 4 H–V diagrams in OEI with $\bar{\Omega}_{\min} = 0.78$.

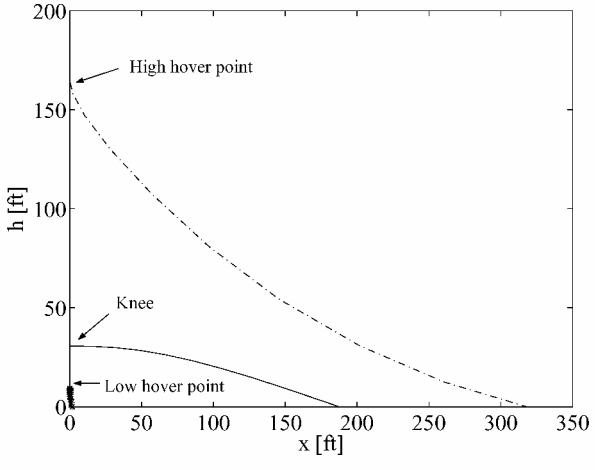

Fig. 5 Optimal landing flights in OEI with engine failures occurring on boundaries of H–V diagram with W = 14,000 lb and $\bar{\Omega}_{\min}$ = 0.78: height vs horizontal distance.

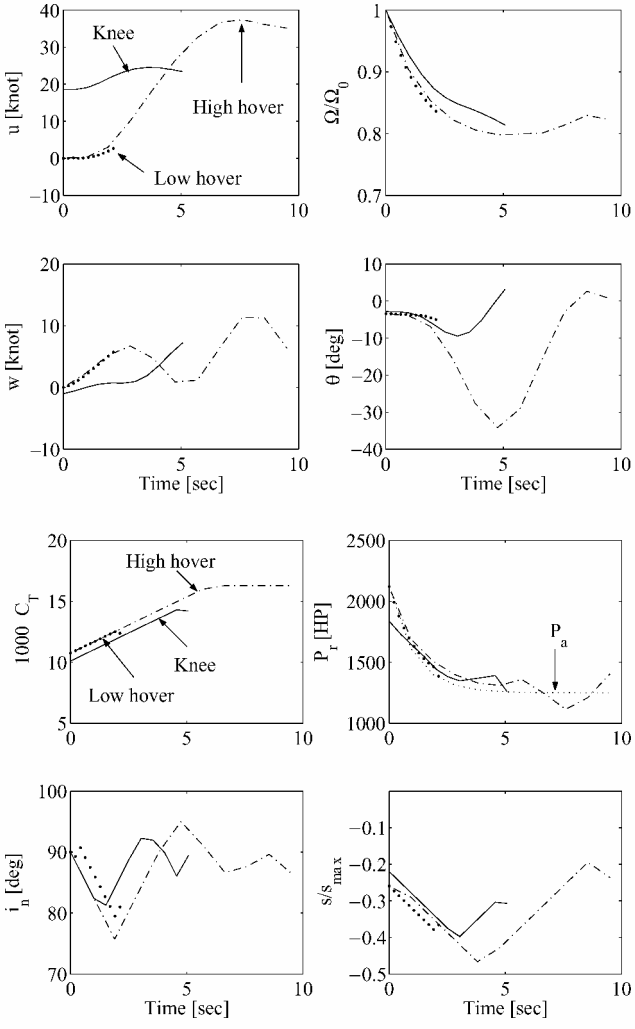

Fig. 6 Optimal landing flights in OEI with engine failures occurring on boundaries of H–V diagram with $W = 14{,}000$ lb and $\bar{\Omega}_{\min} = 0.78$: states and controls.

thrust coefficient increases gradually and stays at the maximum toward the end, causing the rotor speed to drop initially and then to stay at the lower bound. In the middle of the flight, the nacelle angle increases to about 95 deg to restore the aircraft pitch angle and to arrest the vertical sink rate for a safe touchdown.

At the knee point, the height is fairly low, but the initial velocity is sufficient to convert that kinetic energy to thrust in an optimal maneuver. These trajectories are similar in many ways to those in an engine failure at the high-hover point. The aircraft dives to increase forward speed to reduce the power consumption. It then pitches back and uses all rotor speed for thrust to land within specified speed and attitude range.

At the low-hover point, the initial speed is very small or zero, and the height is sufficiently low that all initial energy can be used immediately to slow the descent enough to meet the maximum velocity requirements. The thrust coefficient increases to ensure a soft touchdown, causing the rotor speed to decrease monotonically. The nacelle angle decreases gradually to reduce the power required. This decrease of the nacelle angle results in a small increase in the forward speed. The vertical sink rate increases but stays within the maximum permissible value allowed for a safe touchdown. The pitch angle decreases somewhat but stays within the allowed range.

VII. Optimal Flights with AEI

H–V diagrams in the event of a total engine failure are also studied. Total engine failure of a twin-engined aircraft is a very remote event. The FAA requirement in such a case is simply to maintain control. In other words, the idea is to control the inevitable crash

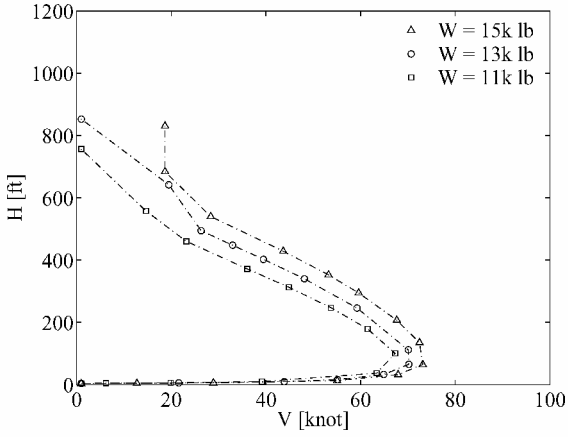

Fig. 7 H–V diagrams in AEI with $\bar{\Omega}_{\min} = 0.6$.

or forced landing. Still, it is of interest to examine unsafe regions and flight characteristics in case of AEI to understand the potential dangers in terminal area operations.

It was quite difficult to calculate the H–V diagram in a total engine failure for a weight of 13,000 lb or higher and a minimum allowed rotor speed of $\bar{\Omega}_{\min} = 0.78$. The normal bell-shaped curve in Fig. 3 was not obtainable. Instead, the heights obtained increase drastically as the κ angle increases to near 90 deg. Similar situations were encountered for much smaller weights.[21] The maximum permissible sink rate at touchdown was even doubled to 20 ff/s, and again, similar results were obtained. These results lead to the discovery that engine failures with low speeds do not allow safe touchdowns in all-engine failure. This is because the rotor moment of inertia for the XV-15 tiltrotor is much less than that of a helicopter. If the rotor speed is allowed to decrease further than the previously stated value of $\bar{\Omega}_{\min} = 0.78$, the situation is improved.

Figure 7 shows H–V diagrams in all-engine failure calculated with $\bar{\Omega}_{\min} = 0.6$. The H–V diagrams in all-engine failure expand in all directions as the gross weight increases. The results do not vary much though with a 4000 lb difference in the gross weight. The size of the H–V diagram is substantial even for the smallest gross weight used: $W = 11{,}000$ lb. In addition, the low-hover points in these H–V diagrams are essentially on the ground, and the knee point speeds are around 70 kn. Therefore, the XV-15 cannot perform vertical takeoff and landing (VTOL) operation if the possibility of all-engine failure is not extremely low, because the tiltrotor speed is small during a VTOL operation. Instead, runway takeoff and landing operations should be used. In a runway takeoff, the tiltrotor accelerates on the ground until a certain liftoff speed and then climbs out. In a runway landing, the tiltrotor touches down on the runway at a certain speed and decelerates on the runway to a stop. Figure 7 indicates that a safe liftoff speed should be of the order of 70 kn (speeds at the knee point in the H–V diagrams).

As with the OEI case, optimal landing trajectories for all-engine failures occurring on the three characteristic points of a H–V diagram are investigated. A nominal gross weight of 13,000 lb is used with $\bar{\Omega}_{\min} = 0.6$. Figures 8 and 9 show a comparison of optimal landing flight trajectories in AEI with engine failures occurring on the high-hover point, the knee point, and the low-hover point of the AEI H–V diagram, respectively. Main features of these trajectories are similar to the corresponding cases in OEI.

For an AEI at the high-hover point, the aircraft initially dives to gain speed and reduce power required. The rotors are then accelerated, and thrust constantly increases. The pitch is flared at the end to decrease the sink rate. For an AEI at the knee point, the trajectories take less time than those from the high-hover point because the aircraft is initially closer to the ground. The thrust is constantly increased. Pitch angle also increases, and the nacelles are tilted back after 2 s to decrease speeds. The power required briefly drops below the zero level to maintain adequate rotor speed and thrust. The low-hover points in AEI H–V diagrams are very low. For an AEI at the low-hover point, all energy is quickly traded

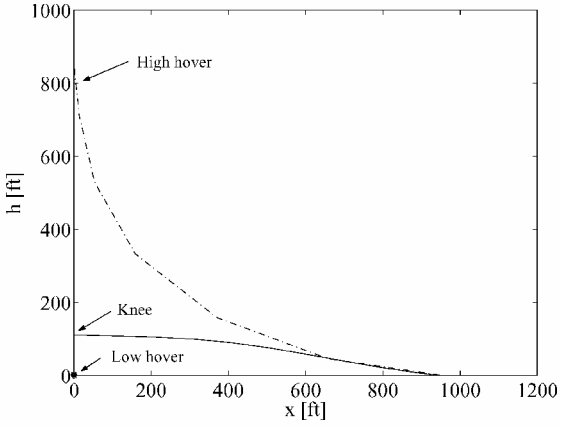

Fig. 8 Optimal landing flights in AEI with engine failures occurring on boundaries of H–V diagram with $W = 13{,}000$ lb and $\bar{\Omega}_{min} = 0.6$: height vs horizontal distance.

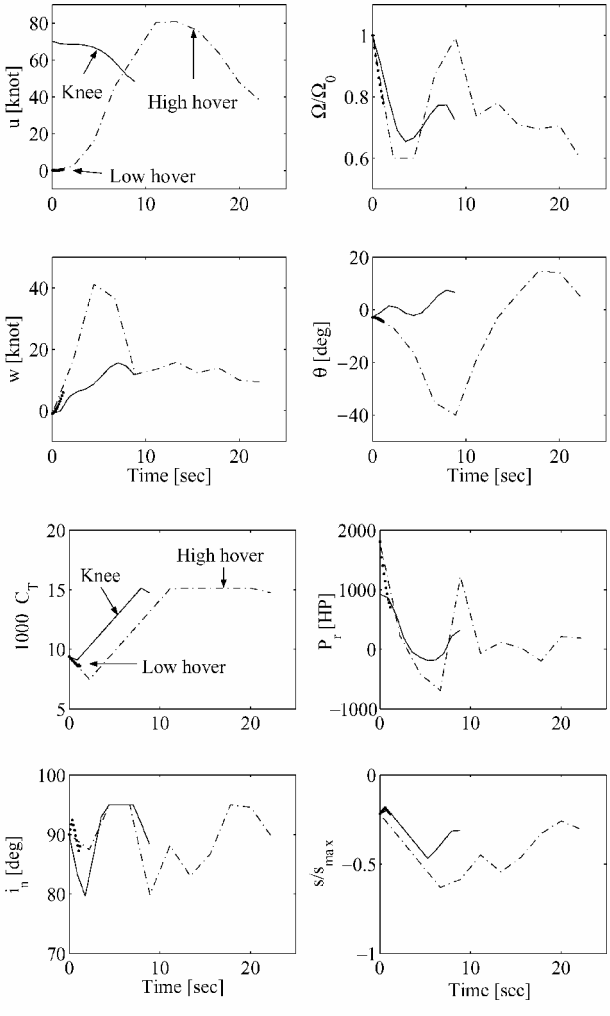

Fig. 9 Optimal landing flights in AEI with engine failures occurring on boundaries of H–V diagram with $W = 13{,}000$ lb and $\bar{\Omega}_{min} = 0.6$: states and controls.

for thrust for the tiltrotor to achieve an acceptable vertical landing speed.

VIII. Sensitivity Analyses

The H–V diagrams determined earlier reveal the inherent abilities of the XV-15 aircraft to survive engine failures. On the other hand, there are various error sources and uncertainties in the numerical optimization process. These errors affect the calculated H–V diagrams in varying degrees. Therefore, these calculated H–V diagrams should only be considered as references for actual H–V diagrams that can be determined via flight tests. Sensitivity analyses are now conducted to examine influences of various modeling errors and uncertainties on the calculated H–V diagrams. These sensitivity analyses are based on an OEI case with $W = 14{,}000$ lb, $\kappa = 40$ deg, $V_c = 0$, and $h_c = 40$ ft.

The collocation method used in this paper is a direct method, which only approximates the true optimal solution. The equations of motion are satisfied approximately with the forward difference evaluated at the midpoint of the interval. As a result, the more nodes used in the optimization, in general, the more accurate the integration approximation becomes. Because this optimization problem is solved repeatedly, the amount of computational time becomes a factor in choosing the number of nodes. The use of 16 nodes is good for the solution accuracy, because increasing to 21 nodes only changes the height by 1.0% and the velocity by 1.5%. The use of 11 nodes also provides a good solution, because increasing to 21 nodes only causes a change in height of 2.8% and a change in velocity of 5.9 %. The use of 11 nodes produces a solution that is not as smooth as the 16-node case, but it takes less than half the time to solve. Table 2 shows that changing the number of nodes only changes the solution by a small amount. In the current paper, all of the H–V diagrams are, therefore, obtained using 11 equally spaced nodes.

The effect of pilot delay is examined in Table 3. As the pilot delay increases from 0.5 to 1.0 s, the H–V diagram height increases by 3.6% and the velocity increases by 7.4%. Pilot actions during the delay period are assumed to hold controls at constant values that are required for steady-state flight before the engine failure. The H–V diagrams shown in operator's manual for each type of helicopter are established by skilled pilots, who try to simulate response actions of average pilots.[25] This is done, in part, by specifying a definite delay time following an engine failure before moving the controls. This delay time depends on specific certification requirements. Table 3 indicates that assumed pilot delay times affect the size of a H–V Diagram significantly.

Effects of model parameter uncertainties are shown in Table 4. The first row shows the results obtained with all nominal values

Table 2 Effect of number of nodes

N	h_0, ft	V_0, kn
11	72.9	14.3
16	71.6	13.7
21	70.9	13.5

Table 3 Effect of pilot delay

Delay, s	h_0, ft	V_0, kn
0.0	71.6	13.7
0.5	83.1	18.8
1.0	86.1	20.2

Table 4 Effects of model parameter uncertainty

Parameter	Nominal	Value used	h_0, ft	V_0, kn
All	Nominal		72.4	14.1
u_{max}	40	60	75.8	15.6
		20	71.0	13.5
K_{ind}	1.10	1.20	82.1	18.3
		1.05	66.7	11.7
c_d	0.015	0.03	84.3	19.3
		0.01	70.6	13.3
η_p	0.95	0.9	78.9	16.9
		1.0	65.7	11.2
η_{ss}	0.75	1.0	72.8	14.3
		0.50	71.9	13.9
η_i	1.5	2.0	73.2	14.5
		1.0	71.8	13.9
η_{hs}	0.9	1.0	72.3	14.1
		0.7	72.6	14.2

used (Appendix). Table 4 indicates that whereas some parameters varying within their bounds have little effect on the solution, other parameters within their bounds have significant effects on the sizes of the calculated H–V diagrams. These effective parameters include the average rotor blade drag coefficient c_d, maximum horizontal speed constraint at touchdown $u_{\max}$, induced flow factor K_{ind}, and the power factor η_p. Essentially, tiltrotor flights after an engine failure are energy management problems. Parameters associated with the power requirement modeling affect the predictions of H–V diagrams. If the H–V diagram results are to be used as benchmarks for flight tests, these effective parameters should be modeled accurately for a particular tiltrotor.

In the preceding results, the optimal nacelle angle control is employed at the maximum rate allowed of 7.5 deg/s, and this constraint is active during the optimal flights. In practice, the pilot may not apply the nacelle angle change at this rate, or may simply hold the nacelle angle at a constant value. In the latter case, an optimal constant nacelle angle may be determined in the optimization process as a parameter. In any case, the H–V diagrams determined with slower or constant nacelle angle control are somewhat larger in sizes than the H–V diagrams determined earlier. The exact changes to the H–V diagrams depend on the allowed maximum nacelle angle rate.

Effects of control rate limits are also studied. A fairly significant difference is observed when increasing control rate limits by 10 times. Therefore, a specific tiltrotor's control rate limits need to be accurately determined in optimization studies.

Finally, the effects of the minimum rotor speed bound $\Omega_{\min}$ are examined. As the lower bound on the rotor speed increases, the H–V diagrams expands at all gross weights.

IX. Conclusions

This paper applies optimal control theories to determine combinations of tiltrotor heights and speeds from which safe landings cannot be made in the event of an engine failure. These combinations form regions known as H–V diagrams for rotorcraft flight. In this paper, a longitudinal rigid-body tiltrotor model is developed, and parameters of the XV-15 tiltrotor aircraft are used. Tabular aerodynamic data of the XV-15 are fit into smooth functions to increase the efficiency of numerical optimizations. An optimal control problem is formulated that minimizes a linear combination of initial height and speed, from which a safe landing can still be made in case of an engine failure. Realistic constraints from tiltrotor performance considerations are imposed, and acceptable ranges of tiltrotor speeds and attitudes at touchdown are specified through terminal constraints. This optimal control problem is converted into a parameter optimization problem via collocation for numerical solutions. It is solved repeatedly to obtain sufficient number of data points on a H–V diagram boundary and to study H–V diagrams for various tiltrotor gross weights. H–V diagrams in both OEI and AEI are studied. Sensitivity analyses are conducted to examine effects of various modeling errors and uncertainties. Optimal landing flights in engine failure occurring on boundaries of H–V diagrams are examined.

Calculated H–V diagrams are similar in shapes to known H–V diagrams for helicopters. In particular, H–V diagrams contract in all directions as the gross weight decreases. H–V diagrams in OEI indicate that the XV-15 tiltrotor can operate in a VTOL mode with a maximum gross weight around 12,000 lb, and in runway operations with greater gross weights. H–V diagrams in all-engine failure have knee speeds around 70 kn at various gross weights. These diagrams indicate that the tiltrotor aircraft can not be used in a VTOL mode if the prospect of all-engine failure is not entirely negligible. In this case, the tiltrotor can only perform a runway operation. Tiltrotor landing flights after engine failure are essentially constrained energy management problems. In all cases, the tiltrotor aircraft tries to reduce its power consumption to the level of the remaining power available and at the same time to satisfy final speed and attitude constraints for a safe touchdown. The sensitivity analyses show that it is important to obtain accurate values for both pilot response delays and model parameters that affect the prediction of power requirements.

X. Appendix: Model Parameters Used in the Optimizations

Main dimensions of the XV-15 tiltrotor aircraft are given in Refs. 1–5. The XV-15 aircraft has a design gross weight of 13,000 lb, a maximum gross weight of 15,000 lb, $R = 12.5$ ft, $\Omega_0 = 61.68$ rad/s, $i_{n,\max} = 95$ deg, $i_{n,\min} = 0$, and $\sigma = 0.089$. Parameters used in the optimizations are selected as follows: $P_{\text{OEI}} = 1250$ hp, $t_p = 0.2$ s, $\theta_{\max} = 40$ deg, $\theta_{\min} = -40$ deg, $h_{\min} = 0$, $C_{T_{\max}} = 0.17\sigma$, $C_{T_{\min}} = 0.0001\sigma$, $K_{\text{ind}} = 1.15$, $f_G = 1.0$, $c_d = 0.015$, $\eta_{\text{ss}} = 0.75$, $\eta_i = 1.5$, $\eta_p = 0.95$, $\eta_{\text{hs}} = 0.9$, $\beta_{\max} = 12$ deg, $\delta_{e_{\max}} = 20$ deg, $(\dot{i}_n)_{\max} = 7.5$ deg/s, $(\mathrm{d}\bar{C}_T/\mathrm{d}\tau)_{\max} = 5.0$, $(\mathrm{d}\bar{s}/\mathrm{d}\tau)_{\max} = 0.5$, $\bar{\Omega}_{\max} = 1.1$, $\bar{\Omega}_{\min} = 0.78$, $\theta_{f,\min} = -5$ deg, $\theta_{f,\max} = 10$ deg, $i_{n_{f,\min}} = 60$ deg, $w_{\max} = 10$ ft/s, and $u_{\max} = 100$ ft/s, $u_{\text{cr}} = 40$ ft/s, $a = 1.386$, $b = 3.114$, and $\delta_{\text{fl}} = 20$ deg.

Acknowledgments

This research was supported by the Rotorcraft Division at NASA Ames Research Center under NCC2-809. We thank William Decker for many valuable comments and thank Robert Chen, William Hindson, and Daniel Dugan for many helpful discussions. We also thank an anonymous reviewer for many careful comments.

References

[1]Dugan, D. C., "Designing the V-22 Tiltrotor: A Flight Test Pilot's Perspective," *Vertiflite*, Vol. 44, No. 3, 1998, pp. 32–36.

[2]Maisel, M. D., "Tilt Rotor Research Aircraft Familiarization Document," NASA TM X-62, 407, Jan. 1975.

[3]Dugan, D. C., Erhart, R. G., and Schroers, L. G., "The XV-15 Tilt Rotor Research Aircraft," NASA TM 81244, Sept. 1980.

[4]Churchill, G. B., and Dugan, D. C., "Simulation of the XV-15 Tilt Rotor Research Aircraft," NASA TM 84222, March, 1982.

[5]Wernicke, K. G., "Performance and Safety Aspects of the XV-15 Tilt Rotor Research Aircraft," *Proceedings of the 33rd Annual National Forum of the American Helicopter Society*, American Helicopter Society, Alexandria, VA, May 1977, pp. 77.33-14-1–77.33-14-9.

[6]Ferguson, S. W., "A Mathematical Model For Real Time Flight Simulation of a Generic Tilt-Rotor Aircraft," NASA CR-166536, Sept. 1988.

[7]Marr, R. L., Willis, J. M., and Churchill, G. B., "Flight Control System Development for the XV-15 Tilt Rotor Aircraft," *Proceedings of the 32nd Annual National Forum of the American Helicopter Society*, American Helicopter Society, Alexandria, VA, May 1976, pp. 1042-1–1042-13.

[8]Pollack, M., Warburton, F., and Curtiss, H. C., "A Simulation Study of Tiltrotor Vertical Takeoff Procedures Using Conventional and Variable Diameter Rotor Systems," *17th European Rotorcraft Forum*, Paper 91-26, Berlin, Germany, Sept. 1991, pp. 91-26.1–91-26.23.

[9]Okuno, Y., Kawachi, K., Azuma, A., and Saito, A., "Analytical Prediction of Height–Velocity Diagram of a Helicopter Using Optimal Control Theory," *Journal of Guidance, Control, and Dynamics*, Vol. 14, No. 2, 1991, pp. 453–459.

[10]Schmitz, F., "Optimal Takeoff Trajectories of a Heavily Loaded Helicopters," *Journal of Aircraft*, Vol. 8, No. 9, 1971, pp. 717–723.

[11]Johnson, W., "Helicopter Optimal Descent and Landing After Power Loss," NASA TM 73244, May 1977.

[12]Lee, A. Y., Bryson, A. E., and Hindson, W. S., "Optimal Landing of a Helicopter in Autorotation," *Journal of Guidance, Control, and Dynamics*, Vol. 11, No. 1, 1988, pp. 7–12.

[13]Okuno, Y., and Kawachi, K., "Optimal Control of Helicopters Following Power Failure," *Journal of Guidance, Control, and Dynamics*, Vol. 17, No. 1, 1991, pp. 181–186.

[14]Okuno, Y., and Kawachi, K.,"Optimal Takeoff of a Helicopter for Category A V/STOL Operations," *Journal of Aircraft*, Vol. 30, No. 2, 1993, pp. 235–240.

[15]Cerbe, T. M., and Reichert, G., "Optimization of Helicopter Takeoff and Landing," *Journal of Aircraft*, Vol. 26, No. 10, 1989, pp. 925–931.

[16]Zhao, Y., and Chen, R. T. N., "Critical Considerations for Helicopters During Runway Takeoffs," *Journal of Aircraft*, Vol. 32, No. 4, 1995, pp. 773–781.

[17]Zhao, Y., Jhemi, A., and Chen, R. T. N., "Optimal VTOL Helicopter Operation in One Engine Failure," *Journal of Aircraft*, Vol. 33, No. 2, 1996, pp. 337–346.

[18]Cerbe, T. M., Reichert, G., and Schrage, D. P., "Short Takeoff Optimization for the XV-15 Tiltrotor Aircraft," *17th European Rotorcraft Forum*, Berlin, Germany, Sept. 1991, pp. 213–232.

[19]Okuno, Y., and Kawachi, K., "Optimal Takeoff Procedures for a Transport Category Tiltrotor," *Journal of Aircraft*, Vol. 30, No. 3, 1993, pp. 291–292.

[20]Carlson, E. B., and Zhao, Y. J., "Optimal Short Takeoff of Tiltrotor Aircraft in One Engine Failure," *Journal of Aircraft*, Vol. 39, No. 2, 2002, pp. 280–289.

[21]Carlson, E. B., "Optimal Tiltrotor Aircraft Operations During Power Failure," Ph.D. Dissertation, Dept. of Aerospace Engineering and Mechanics, Univ. of Minnesota, Minneapolis, MN, July 1999.

[22]Talbot, P. D., Tinling, B. E., Decker, W. A., and Chen, R. T. N., "A Mathematical Model of a Single Main Rotor Helicopter for Piloted Simulation," NASA TM-84281, Sept. 1982.

[23]Johnson, W., *Helicopter Theory*, Princeton Univ. Press, Princeton, NJ, 1980, pp. 282–283.

[24]Stepniewski, W. Z., and Keys, C. N., *Rotary-Wing Aerodynamics*, Dover, New York, 1984, Chaps. 2 and 3.

[25]Prouty, R. W., *Helicopter Aerodynamics*, PJS Publications Inc., Peoria, IL, 1985, p. 80.

[26]Betts, J., "Survey of Numerical Methods for Trajectory Optimization," *Journal of Guidance, Control, and Dynamics*, Vol. 21, No. 2, 1998, pp. 193–207.

[27]Hull, D., "Conversion of Optimal Control Problems Into Parameter Optimization Problems," *Journal of Guidance, Control, and Dynamics*, Vol. 20, No. 1, 1997, pp. 57–60.

[28]Herman, A. L., and Conway, B. A., "Direct Optimization Using Collocation Based on High-Order Gauss–Lobatto Quadrature Rules," *Journal of Guidance, Control, and Dynamics*, Vol. 19, No. 3, 1996, pp. 592–599.

[29]Gill, P. E., Murray, W., Saunders, M. A., and Wright, M. H., "User's Guide for NPSOL (Version 4.0): A Fortran Package for Nonlinear Programming," Dept. of Operations Research, Stanford University, CA, TR SOL 86-2, Jan. 1986.